Internal wave focusing by annular forcing

Bruno Voisin

Internal wave focusing by annular forcing

Bruno Voisin

Laboratoire des Écoulements Géophysiques et Industriels,
CNRS & Université Grenoble Alpes, France
bruno.voisin@legi.cnrs.fr

Abstract

A linear theory is proposed for the focusing of internal waves generated by the oscillations of a horizontal annulus that is slender, namely of large aspect ratio, but otherwise arbitrary. The theory exploits the separation of scales and is applied to two configurations: a circular torus, and circular Gaussian topography at the ocean bottom. Both complete and partial annuli are considered. Focusing takes place in all cases, irrespective of the criticality of the forcing, implying that horizontal curvature is the key ingredient. The theory compares quantitatively with recent experiments for a torus.

1 Introduction

A common cause of dissipation in stratified and/or rotating fluids is the accumulation of internal and/or inertial waves in a finite domain, leading to ultimate breaking. Such accumulation takes place when wave beams intersect. In two dimensions the beams may be either separate (Smith and Crockett, 2014) or an incident beam and its reflection at a surface (Grisouard et al., 2013). In three dimensions a new possibility arises, the self-focusing of a beam owing to its conical geometry. The occurrence of 'focusing singularities' has first been noticed for the oscillations of a sphere (Appleby and Crighton, 1987), a circular ring (Simakov, 1993) and a circular disk (Tilgner, 2000), then studied in greater detail for circular Gaussian topography at the ocean bottom (Bühler and Muller, 2007) and again for the disk (Le Dizès, 2015). The reality of focusing has been demonstrated experimentally and numerically with a circular torus in a rotating fluid by Duran-Matute et al. (2013). Axisymmetry is not mandatory though, and focusing arises also for elliptical (Bühler and Muller, 2007) or horseshoe-shaped (Grisouard and Bühler, 2012) topography. As a rule, the efficiency of focusing is set by the order of tangency of the wave generator to the characteristic cone with apex at the focus (Simakov, 1994). We present a linear theory of internal wave focusing by the oscillations of a slender circular annulus of vertical axis and azimuthally varying cross section. The theory is applied to a torus and to circular Gaussian topography, then compared with recent experiments for the torus by Ermanyuk et al. (2016).

2 General theory

A rigid circular annulus of vertical z-axis and major radius b, shown in figure 1, oscillates at the frequency $\omega < N$ and velocity $\boldsymbol{u}_0 \mathrm{e}^{-\mathrm{i}\omega t} = (u_0, v_0, w_0)\mathrm{e}^{-\mathrm{i}\omega t}$ in a uniformly stratified fluid of buoyancy frequency N and kinematic viscosity ν. The annulus may vary azimuthally, its cross-section having a characteristic minor radius a. Internal gravity waves are generated, which propagate at the angle $\theta = \arccos(\omega/N)$ to the vertical while attenuating at the rate $\beta\kappa^3$ per unit distance along rays, with κ the wavenumber and $\beta = \nu/(2\omega\tan\theta)$. The problem is ruled by the nondimensional parameters

$$\Omega = \frac{\omega}{N}, \quad \epsilon = \frac{b}{a}, \quad St = \frac{\omega a^2}{\nu}, \quad Ke = \frac{|\boldsymbol{u}_0|}{\omega a}, \tag{1}$$

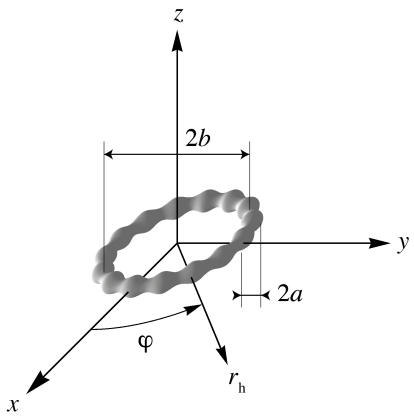

Figure 1: Geometry and notations for an azimuthally modulated annulus.

respectively the frequency ratio Ω of the waves, the aspect ratio ϵ of the annulus, the Stokes number $St \gg 1$ characterizing the viscous effects, assumed small, and the Keulegan–Carpenter number $Ke \ll 1$ characterizing the nonlinear effects, assumed negligible.

We adopt the approach of Voisin (2003), already applied to an oscillating sphere by Voisin et al. (2011), and represent the annulus as a source of mass releasing the volume $q\mathrm{e}^{-\mathrm{i}\omega t}$ of fluid per unit volume per unit time. In cylindrical coordinates $(r_\mathrm{h}, \varphi, z)$, the vertical velocity disturbance is given by

$$w = \frac{\cos^2\theta}{8\pi^2}\mathrm{e}^{-\mathrm{i}\omega t}\,\mathrm{sign}\,z\int_{-\pi}^{\pi}\mathrm{d}\varphi_k\int_0^\infty \mathrm{d}\kappa\,\kappa q(\kappa_\mathrm{h}=\kappa\cos\theta,\varphi_k,m=-\kappa\sin\theta\,\mathrm{sign}\,z) \times\exp\left(-\frac{\beta\kappa^3|z|}{\cos\theta}\right)\exp\{\mathrm{i}\kappa[r_\mathrm{h}\cos\theta\cos(\varphi_k-\varphi)-|z|\sin\theta]\}, \quad (2)$$

and similarly for the other velocity components, with

$$q(\boldsymbol{k}) = \int q(\boldsymbol{x})\mathrm{e}^{-\mathrm{i}\boldsymbol{k}\cdot\boldsymbol{x}}\,\mathrm{d}^3x \quad (3)$$

the spectrum of the forcing. The annulus is assumed slender, namely of large aspect ratio $\varepsilon \gg 1$, so that each section behaves as an independent two-dimensional wave generator, for which the most generic representation is, in local Cartesian coordinates (x', z),

$$q(x',z) = u_0'\frac{\partial}{\partial x'}f(x',z) + w_0\frac{\partial}{\partial z}g(x',z), \quad (4)$$

with f and g integrable so as to ensure, in particular, no net source outflow $\int q\,\mathrm{d}x'\,\mathrm{d}z = 0$. The representation of the annulus follows as

$$q(r_\mathrm{h},\varphi,z) = \left(u_0\frac{\partial}{\partial x}+v_0\frac{\partial}{\partial y}\right)f(r_\mathrm{h}-b,z;\varphi) + w_0\frac{\partial}{\partial z}g(r_\mathrm{h}-b,z;\varphi), \quad (5)$$

and its spectrum as

$$q(\kappa_\mathrm{h},\varphi_k,m) = \pi\sum_{n=-\infty}^{\infty}(-\mathrm{i})^n\mathrm{e}^{\mathrm{i}n\varphi_k}\int_0^\infty \mathrm{d}r_\mathrm{h}\,r_\mathrm{h}\Big[2\mathrm{i}w_0 m J_n(\kappa_\mathrm{h}r_\mathrm{h})g_n(r_\mathrm{h}-b,m) + \sum_{\pm}(\mathrm{i}v_0\pm u_0)\kappa_\mathrm{h}J_{n\pm1}(\kappa_\mathrm{h}r_\mathrm{h})f_{n\pm1}(r_\mathrm{h}-b,m)\Big], \quad (6)$$

where we have introduced the Bessel functions J_n and the azimuthal Fourier coefficients

$$f_n(x',z) = \frac{1}{2\pi}\int_{-\pi}^{\pi} f(x',z;\varphi)\mathrm{e}^{-\mathrm{i}n\varphi}\,\mathrm{d}\varphi. \tag{7}$$

To proceed further, we exploit the scale separation associated with the slenderness assumption. At the global scale $\kappa b = O(1)$, the annulus reduces to a ring of dipoles and the Bessel functions may be replaced by their expansion at $r_\mathrm{h} = b$, namely

$$\kappa_\mathrm{h} r_\mathrm{h} J_n(\kappa_\mathrm{h} r_\mathrm{h}) \sim \kappa_\mathrm{h} b J_n(\kappa_\mathrm{h} b) - \kappa_\mathrm{h}(r_\mathrm{h}-b)[\kappa_\mathrm{h} b J_{n+1}(\kappa_\mathrm{h} b) - (n+1)J_n(\kappa_\mathrm{h} b)]. \tag{8}$$

Conversely, at the local scale $\kappa a = O(1)$, the annulus is so big that, in a given azimuthal plane, only the two cross sections from that plane contribute to the radiation while the other cross sections interfere destructively. The Bessel functions may be replaced by their asymptotic expansion for $\kappa_\mathrm{h} r_\mathrm{h} \gg 1$, namely

$$\kappa_\mathrm{h} r_\mathrm{h} J_n(\kappa_\mathrm{h} r_\mathrm{h}) \sim \left(\frac{2}{\pi}\kappa_\mathrm{h} b\right)^{1/2} \cos\left(\kappa_\mathrm{h} r_\mathrm{h} - \frac{\pi}{4} - n\frac{\pi}{2}\right). \tag{9}$$

Comparison of these two singular limits suggests the uniform expansion

$$\begin{aligned} q(\kappa_\mathrm{h},\varphi_k,m) \sim{}& \pi b \sum_{n=-\infty}^{\infty} (-\mathrm{i})^n \mathrm{e}^{\mathrm{i}n\varphi_k} \\ &\times \left\{ 2\mathrm{i}w_0 m \left[J_n(\kappa_\mathrm{h} b) g_n^{(\mathrm{c})} - \left(J_{n+1}(\kappa_\mathrm{h} b) - (n+1)\frac{J_n(\kappa_\mathrm{h} b)}{\kappa_\mathrm{h} b}\right) g_n^{(\mathrm{s})}\right] \right. \\ &\left. + \sum_{\pm} (\mathrm{i}v_0 \pm u_0)\kappa_\mathrm{h} \left[J_{n\pm1}(\kappa_\mathrm{h} b) f_{n\pm1}^{(\mathrm{c})} \pm \left(J_n(\kappa_\mathrm{h} b) - n\frac{J_{n\pm1}(\kappa_\mathrm{h} b)}{\kappa_\mathrm{h} b}\right) f_{n\pm1}^{(\mathrm{s})}\right]\right\}, \end{aligned} \tag{10}$$

where the two-dimensional Fourier transforms

$$f_n^{(\mathrm{c,s})}(k',m) = \int \mathrm{d}x' \int \mathrm{d}z\; f_n(x',z)(\cos,\sin)(k'x')\mathrm{e}^{-\mathrm{i}mz} \tag{11}$$

are evaluated implicitly at (κ_h, m). The separation of the cosine and sine transforms with respect to x' separates the original functions into their even and odd parts, respectively. In the following, only even functions will be considered. The vertical velocity follows from (2) as

$$\begin{aligned} w = \frac{b}{4}\cos^2\theta \mathrm{e}^{-\mathrm{i}\omega t}\,\mathrm{sign}\, z \int_0^\infty \mathrm{d}\kappa\, \kappa^2 \exp\left(-\frac{\beta\kappa^3|z|}{\cos\theta}\right)\exp(-\mathrm{i}\kappa|z|\sin\theta) \\ \times \sum_{n=-\infty}^{\infty} A_n(\kappa) J_n(\kappa r_\mathrm{h}\cos\theta)\mathrm{e}^{\mathrm{i}n\varphi}, \end{aligned} \tag{12}$$

where the functions $f_n^{(\mathrm{c,s})}$ and $g_n^{(\mathrm{c,s})}$ in the coefficients

$$\begin{aligned} A_n(\kappa) = {}& \sum_{\pm} (\mathrm{i}v_0 \pm u_0)\cos\theta \left\{ J_{n\pm1}(\kappa b\cos\theta) f_{n\pm1}^{(\mathrm{c})} \right. \\ &\left. \pm \left[J_n(\kappa b\cos\theta) - n\frac{J_{n\pm1}(\kappa b\cos\theta)}{\kappa b\cos\theta}\right] f_{n\pm1}^{(\mathrm{s})}\right\} - 2\mathrm{i}w_0 \sin\theta\,\mathrm{sign}\, z \\ &\times \left\{ J_n(\kappa b\cos\theta) g_n^{(\mathrm{c})} - \left[J_{n+1}(\kappa b\cos\theta) - (n+1)\frac{J_n(\kappa b\cos\theta)}{\kappa b\cos\theta}\right] g_n^{(\mathrm{s})}\right\} \end{aligned} \tag{13}$$

are evaluated implicitly at $(\kappa_\mathrm{h} = \kappa\cos\theta, m = -\kappa\sin\theta\,\mathrm{sign}\, z)$.

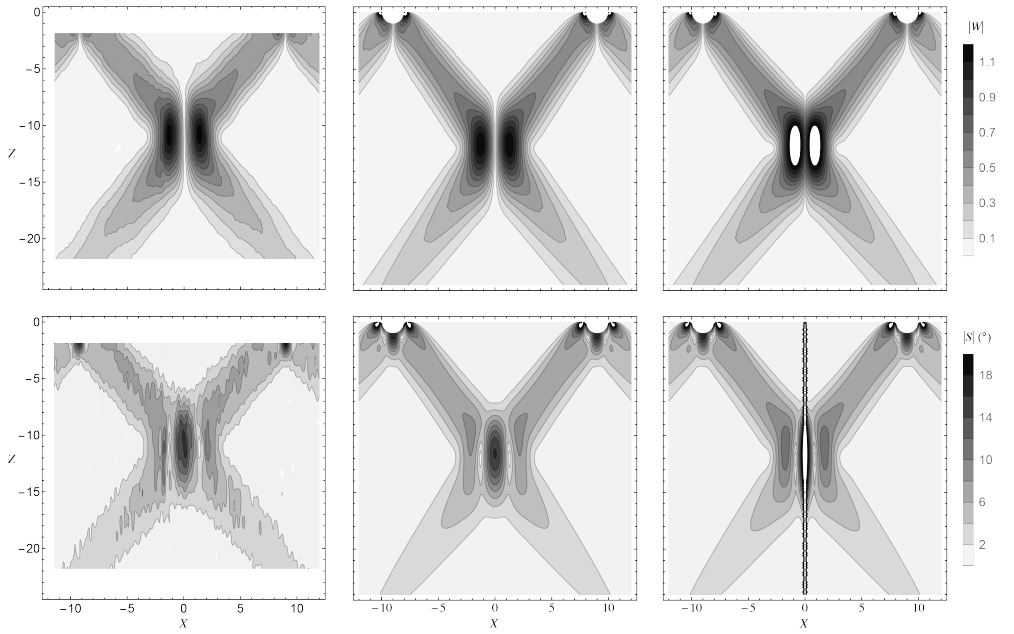

Figure 2: Amplitudes of the vertical velocity (top row) and isopycnal slope (bottom row) in the vertical plane $Y = 0$ for a torus of $\varepsilon = 9$ at $\Omega = 0.80$, $St = 120$ and $Ke = 0.19$, corresponding to case A from Ermanyuk et al. (2016). Their experimental data (left column) are compared with the present three-dimensional theory (middle column) and their quasi-two-dimensional theory (right column).

3 Complete focusing

The analysis is applied first to a torus of circular cross section, oscillating at the velocity $u_0 \mathrm{e}^{-\mathrm{i}\omega t}$ along the x-axis. The boundary integral approach used for the sphere in Voisin et al. (2011) gives

$$f(x', z) = -(1 + \mathrm{i}\tan\theta) H\left(a - \sqrt{x'^2 + z^2}\right), \tag{14}$$

with H the Heaviside step function. All the Fourier coefficients are 0 but

$$f_0^{(\mathrm{c})}(k', m) = -2\pi a(1 + \mathrm{i}\tan\theta)\frac{J_1\left(\sqrt{k'^2 + m^2}a\right)}{\sqrt{k'^2 + m^2}}, \tag{15}$$

and the vertical velocity becomes

$$w = \pi a b u_0 \mathrm{e}^{\mathrm{i}\theta}\cos^2\theta \mathrm{e}^{-\mathrm{i}\omega t}\cos\varphi \operatorname{sign} z \int_0^\infty \exp\left(-\frac{\beta\kappa^3|z|}{\cos\theta}\right) \times \kappa J_1(\kappa a) J_0(\kappa b\cos\theta) J_1(\kappa r_\mathrm{h}\cos\theta)\exp(-\mathrm{i}\kappa|z|\sin\theta)\,\mathrm{d}\kappa. \tag{16}$$

This result is plotted in figure 2 in nondimensional form, namely for $W = w/u_0$ in terms of $(X, Y, Z) = (x, y, z)/a$, in the vertical plane of oscillation $Y = 0$, and compared with the measurements and quasi-two-dimensional model of Ermanyuk et al. (2016). The isopycnal slope $S_x = (\mathrm{i}/\omega)(\partial w/\partial x) = \mathrm{i}Ke(\partial W/\partial X)$ is also plotted. Singularities arise along the line $Z = 0$ at the intersections of the critical rays tangent to the cross sections of the torus. This local inconsistency of the general theory (2), already visible for the sphere in figures 6 and 7 of Voisin et al. (2011), does not affect the rest of the wave field. Initially, the waves propagate away from the cross sections as if from separate cylinders, in beams of decreasing amplitude owing to viscous attenuation. Rapidly, focusing manifests itself and the amplitude increases,

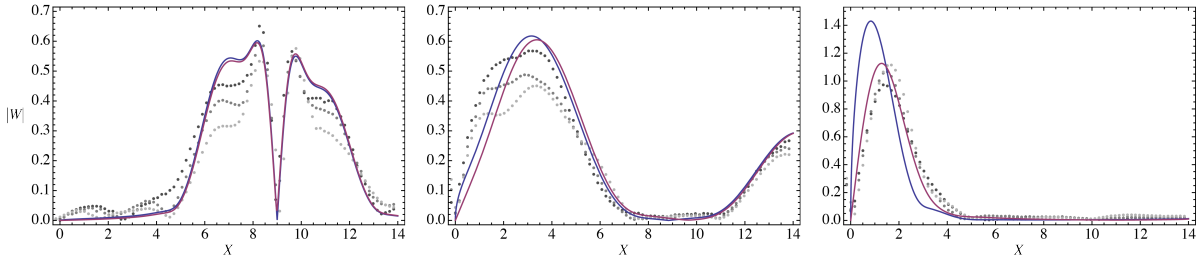

Figure 3: Vertical velocity amplitude profiles in the conditions of figure 2 at $Z = -1.84$ (left), -7.17 (middle) and -12.51 (right). The lines represent the present theory (red) and the quasi-two-dimensional theory (blue), and the dots the experimental points at $Ke = 0.19$ (dark grey), 0.41 (medium grey) and 0.65 (light grey).

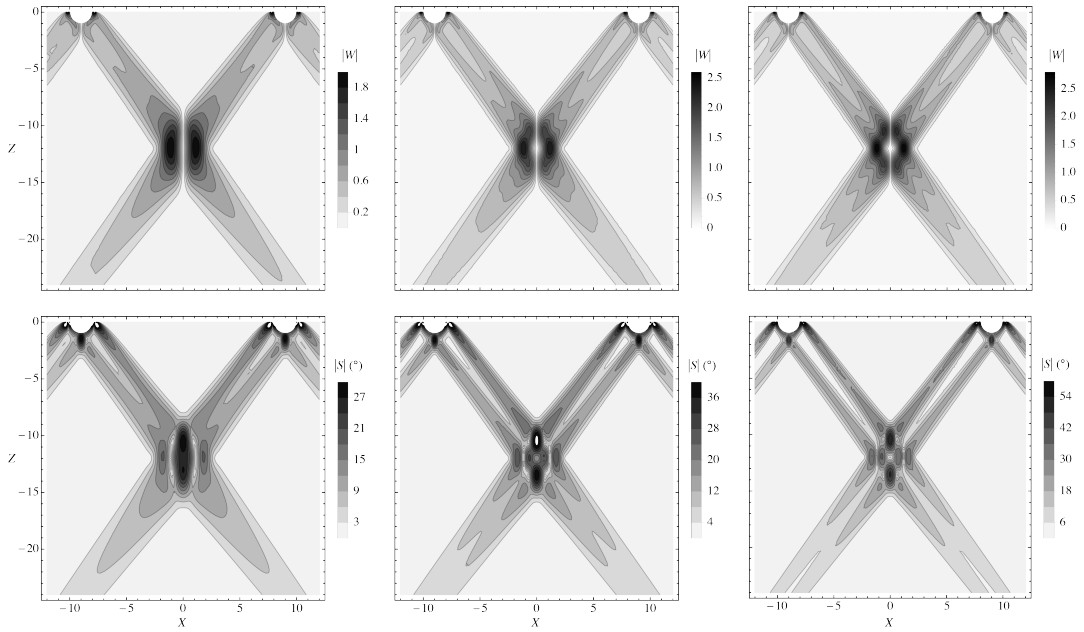

Figure 4: Amplitudes of the vertical velocity (top row) and isopycnal slope (bottom row) in the plane $Y = 0$ at $St = 470$ (left column), 1100 (middle column) and 1900 (right column), corresponding to the multiplication of a by 2, 3 and 4, respectively, compared with figure 2.

to reach a maximum in the biconical region of intersection of the beams. There, the gradients are strong and the isopycnal slopes up to 20°. Once this focal region is traversed, the waves decrease again.

The quasi-two-dimensional model is seen to be valid away from the axis of symmetry and to fail close to this axis, including in the focusing region, where it yields infinite slope. It also gives infinite horizontal velocity at the axis. The comparison is made more quantitative in figure 3, which plots the horizontal wave profiles shortly after the torus, across the focusing region and in-between. The validity of the present linear model is confirmed at $Ke = 0.19$, consistent with previous observations for the sphere (Voisin et al., 2011).

The above results have been obtained at moderate $St = 120$, in a regime were the wave beams are unimodal and their dynamics set by viscosity. As St increases and inviscid dynamics takes over, the beams become bimodal and involve smaller structures and stronger gradients. Figure 4 shows this evolution up to $St = 1900$, at which the slopes reach 60° sufficient for overturning and breaking. This led to the design of the experiments by Shmakova et al. (2016), involving a big torus of diameter 1.5 m and aspect ratio 5 in the 13 m-diameter Coriolis platform.

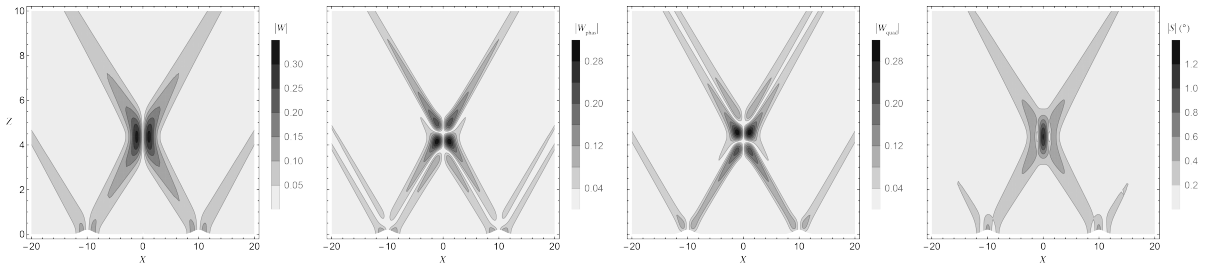

Figure 5: Amplitudes of the vertical velocity (left) and isopycnal slope (right) in the vertical plane $Y = 0$ for circular Gaussian topography of $\varepsilon = 10$ and $h_0/a = 0.2$ at $\Omega = 0.4$, $St = \infty$ and $Ke = 0.04$. These parameters combine the circular geometry from Bühler and Muller (2007) with the 'average' seamount from Llewellyn Smith and Young (2002). For the velocity the amplitudes of the in-phase component $W_{\mathrm{phas}} = \mathrm{Re}[W\mathrm{e}^{\mathrm{i}\omega t}]$ (middle left) and quadrature component $W_{\mathrm{quad}} = \mathrm{Im}[W\mathrm{e}^{\mathrm{i}\omega t}]$ (middle right) are also plotted separately.

Another type of forcing, closer to oceanic conditions, is barotropic flow at the velocity $-u_0\mathrm{e}^{-\mathrm{i}\omega t}$ along the x-axis over circular bottom topography of profile $h(x')$. On the common assumption that the slope is infinitesimal, namely $|\mathrm{d}h/\mathrm{d}x'| \ll 1$, linearization of the boundary condition yields $f(x', z) = 2h(x')\delta(z)$. Like Bühler and Muller (2007), we consider a Gaussian profile $h(x') = h_0 \exp[-x'^2/(2a^2)]$ of height h_0 and standard deviation a, for which

$$f(x', z) = 2h_0 \exp\left(-\frac{x'^2}{2a^2}\right)\delta(z), \quad f_0^{(\mathrm{c})}(k', m) = 2\sqrt{2\pi}ah_0 \exp\left(-\frac{k'^2a^2}{2}\right), \qquad (17,18)$$

and all the other Fourier coefficients 0. The vertical velocity follows as

$$w = -\sqrt{2\pi}abh_0u_0 \cos^3\theta \mathrm{e}^{-\mathrm{i}\omega t} \cos\varphi \,\mathrm{sign}\, z \int_0^\infty \exp\left(-\frac{\beta\kappa^3|z|}{\cos\theta}\right) \times \kappa^2 \exp\left(-\frac{\kappa^2a^2\cos^2\theta}{2}\right) J_0(\kappa b\cos\theta) J_1(\kappa r_{\mathrm{h}}\cos\theta) \exp(-\mathrm{i}\kappa|z|\sin\theta)\,\mathrm{d}\kappa, \quad (19)$$

and is represented in figure 2 for average oceanic parameters. Focusing remains present, with amplitudes an order of magnitude smaller than for the torus owing to the smaller $Ke = 0.04$. Separate plots of the in-phase and quadrature amplitudes exhibit the same upside-down vertical symmetry on either side of the focal point ($r_{\mathrm{h}} = 0, z = b\cot\theta$) as seen by Bühler and Muller (2007), with a different structure given the different types of forcing, monopolar for Bühler and Muller (2007) and dipolar here.

4 Partial focusing

When only part of the circular annulus is present, focusing becomes incomplete. For the torus, truncation to azimuthal breadth $\Phi - \Delta\Phi < \varphi < \Phi + \Delta\Phi$ multiplies (14) by

$$H(\Delta\Phi - |\varphi - \Phi|) = \sum_{n=-\infty}^{\infty} \frac{\sin(n\Delta\Phi)}{n\pi}\mathrm{e}^{\mathrm{i}n(\varphi-\Phi)}, \qquad (20)$$

with results shown in figure 6 for half- and quarter-tori in various orientations. Focusing remains present in all cases, with reduced efficiency. For Gaussian topography, Grisouard and Bühler (2012) introduced a smoother truncation, multiplying (17) by

$$\cos^2\left(\frac{\varphi-\Phi}{2}\right) = \frac{1}{2} + \frac{\mathrm{e}^{\mathrm{i}(\varphi-\Phi)}}{4} + \frac{\mathrm{e}^{-\mathrm{i}(\varphi-\Phi)}}{4}, \qquad (21)$$

therefore turning the topography into a horseshoe-shaped one, with results shown in figure 7. Compared with the half-torus, the edge effects are less pronounced.

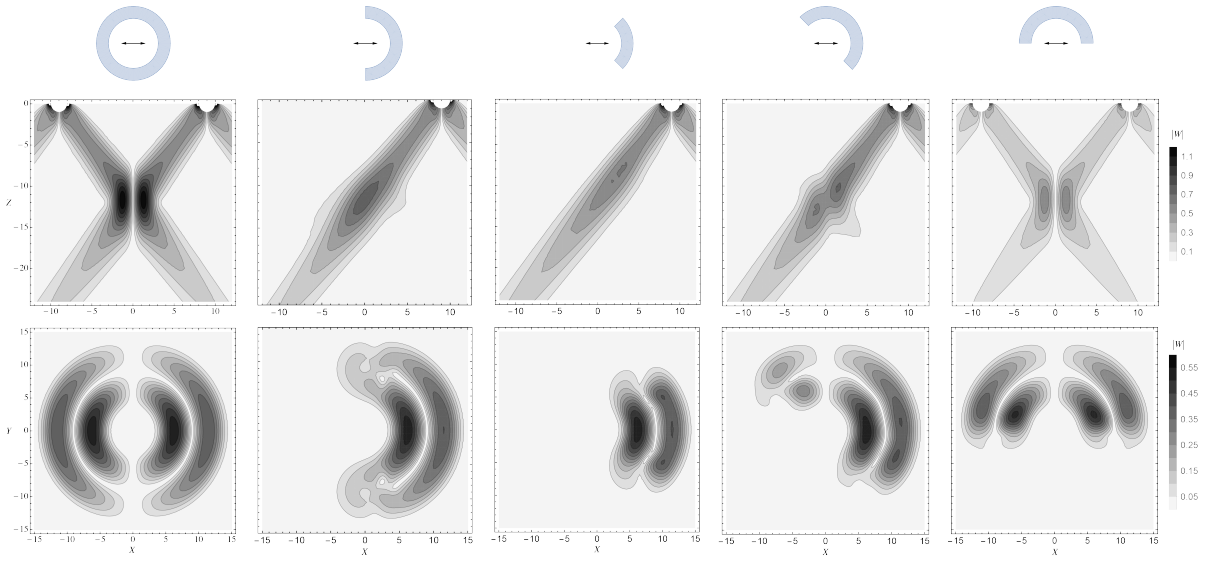

Figure 6: Vertical velocity amplitude in the vertical plane $Y = 0$ (middle row) and horizontal plane $Z = -3.6$ (bottom row) in the conditions of figure 2, for full, quarter- and half-tori in various configurations (top row).

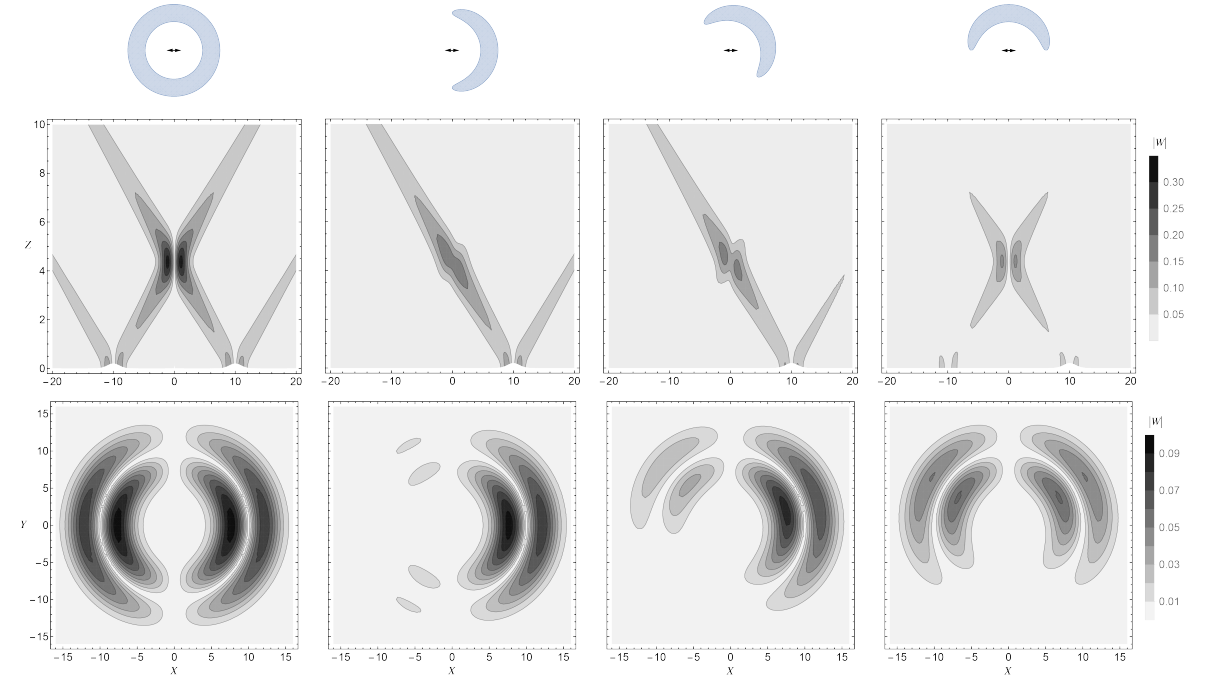

Figure 7: Vertical velocity amplitude in the vertical plane $Y = 0$ (middle row) and horizontal plane $Z = 1$ (bottom row) in the conditions of figure 5, for various circular and horseshoe-shaped topographies (top row).

5 Conclusions

Slender annular forcing, whether supercritical like the torus or subcritical like flat Gaussian topography, has been seen to focus internal waves effectively. Focusing remains significant also when the annulus is incomplete. Both statements imply that horizontal curvature is the key ingredient, consistent with the observation, both in the laboratory (Mercier et al., 2013) and in the field (Buijsman et al., 2014), than even slight horizontal curvature of the bottom topography yields noticeable wave amplification.

Acknowledgements

Jan-Bert Flór and Evgeny Ermanyuk are thanked for presenting this problem as one that needed a solution, and for suggesting the slender-body approach. Together with Natalia Shmakova, they are thanked for providing access to their experimental data. This work has been supported by grants from Labex OSUG@2020 (Investissements d'avenir – ANR10 LABX56) and the Del Duca Foundation of the Institut de France.

References

Appleby, J. C. and Crighton, D. G. (1987). Internal gravity waves generated by oscillations of a sphere. *J. Fluid Mech.*, 183:439–450.

Bühler, O. and Muller, C. J. (2007). Instability and focusing of internal tides in the deep ocean. *J. Fluid Mech.*, 588:1–28.

Buijsman, M. C., Klymak, J. M., Legg, S., Alford, M. H., Farmer, D., MacKinnon, J. A., Nash, J. D., Park, J.-H., Pickering, A., and Simmons, H. (2014). Three-dimensional double-ridge internal tide resonance in Luzon Strait. *J. Phys. Oceanogr.*, 44:850–869.

Duran-Matute, M., Flór, J.-B., Godeferd, F. S., and Jause-Labert, C. (2013). Turbulence and columnar vortex formation through inertial-wave focusing. *Phys. Rev.* E, 87:041001.

Ermanyuk, E. V., Shmakova, N. D., and Flór, J.-B. (2016). Internal wave focusing by a horizontally oscillating torus. *J. Fluid Mech.* (submitted).

Grisouard, N. and Bühler, O. (2012). Forcing of oceanic mean flows by dissipating internal tides. *J. Fluid Mech.*, 708:250–278.

Grisouard, N., Leclair, M., Gostiaux, L., and Staquet, C. (2013). Large scale energy transfer from an internal gravity wave reflecting on a simple slope. *Procedia IUTAM*, 8:119–128.

Le Dizès, S. (2015). Wave field and zonal flow of a librating disk. *J. Fluid Mech.*, 782:178–208.

Llewellyn Smith, S. G. and Young, W. R. (2002). Conversion of the barotropic tide. *J. Phys. Oceanogr.*, 32:1554–1566.

Mercier, M. J., Gostiaux, L., Helfrich, K., Sommeria, J., Viboud, S., Didelle, H., Ghaemsaidi, S. J., Dauxois, T., and Peacock, T. (2013). Large-scale, realistic laboratory modeling of M_2 internal tide generation at the Luzon Strait. *Geophys. Res. Lett.*, 40:5704–5709.

Shmakova, N., Flór, J.-B., Voisin, B., Sommeria, J., and Viboud, S. (2016). High Stokes number wave focusing by a circular ridge: Internal, inertial and inertia–gravity waves. *This conf.*

Simakov, S. T. (1993). Initial and boundary value problems of internal gravity waves. *J. Fluid Mech.*, 248:55–65.

Simakov, S. T. (1994). Formation of singularities of limiting amplitude in a density stratified fluid disturbed by an extended monochromatic forcing. *Wave Motion*, 19:11–27.

Smith, S. and Crockett, J. (2014). Experiments on nonlinear harmonic wave generation from colliding internal wave beams. *Exp. Therm. Fluid Sci.*, 54:93–101.

Tilgner, A. (2000). Oscillatory shear layers in source driven flows in an unbounded rotating fluid. *Phys. Fluids*, 12:1101–1111.

Voisin, B. (2003). Limit states of internal wave beams. *J. Fluid Mech.*, 496:243–293.

Voisin, B., Ermanyuk, E. V., and Flór, J.-B. (2011). Internal wave generation by oscillation of a sphere, with application to internal tides. *J. Fluid Mech.*, 666:308–357.